

# Exposure of engineered nanoparticles to human lung epithelial cells: Influence of chemical composition and catalytic activity on oxidative stress

*Ludwig K. Limbach<sup>1</sup>, Peter Wick<sup>2</sup>, Pius Manser<sup>2</sup>, Robert N. Grass<sup>1</sup>, Arie Bruinink<sup>2</sup>,  
Wendelin J. Stark<sup>1,\*</sup>*

<sup>1</sup> Institute for Chemical and Bioengineering, Department of Chemistry and Applied Biosciences, ETH Zurich, CH-8093 Zurich, Switzerland

<sup>2</sup> Empa, Swiss Federal Laboratories for Materials Testing and Research, Laboratory for Material-Biology Interactions, Lerchenfeldstrasse 5, CH-9014 St. Gallen, Switzerland

## ***Supplementary Information***

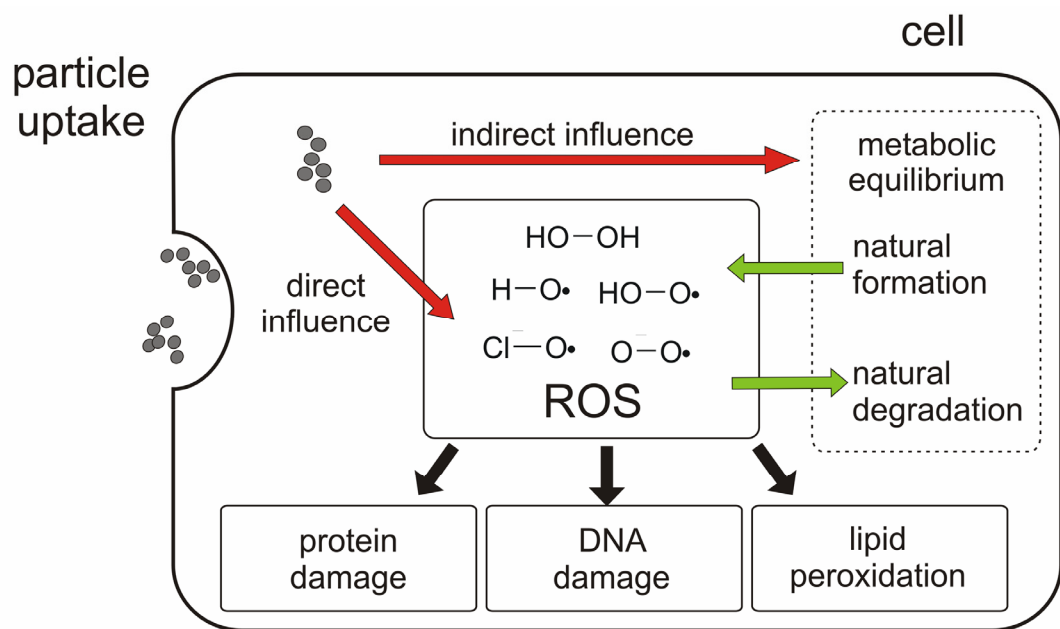
\*Correspondence should be addressed to

Wendelin J. Stark  
Institute for Chemical and Bioengineering, HCI E 107  
ETH Zurich  
Wolfgang-Pauli-Str. 10  
CH-0893 Zurich  
Switzerland

e-mail: [wendelin.stark@chem.ethz.ch](mailto:wendelin.stark@chem.ethz.ch)  
phone: +41 44 632 09 80  
fax: +41 44 633 10 83.

## Supporting information on oxidative stress

Oxidative stress arises from a serious imbalance between the production of reactive oxidizing species and their degradation by the antioxidant defense system in organisms (1). Such reactive oxygen species (ROS) naturally result out of the respiratory chain (2) where their damaging action is confined by a series of enzymes (3) (i.e. catalase, superoxide dismutase). Increased ROS levels were suspected for promoting aging (4) and Alzheimer's disease (5,6) and observed in high glucose condition (i.e. hyperglycemia) (7) leading to damage on mitochondria (8). ROS have also been suspected to activate apoptosis (9) and play an important role in multistage carcinogenesis (10). The natural, intracellular equilibrium between ROS formation and degradation may be disturbed by intracellularly located nanoparticles (Supplementary Figure S1). A direct influence may arise from the production of ROS on the catalytically active surface of the particles or by the action of digested reactive ions. An indirect increase of ROS may arise from stimulation or inhibition of the ROS degradation pathway.



*Supplementary Figure S1. Schematic representation of a cell showing two alternative ways how nanoparticles may affect the intracellular ROS level. The catalytic activity of a nanomaterial may directly contribute to the production of ROS (direct influence). Changes in the natural equilibrium of ROS formation and degradation may also affect the ROS level if nanoparticles interact with signaling pathways, metabolites or other cell constituents (indirect pathway).*

## Materials and methods

*Nanoparticle preparation and dispersion.* All investigated nanoparticles were prepared following exactly the same procedure: Flame spray synthesis (11-13) of mixtures of transition metals dissolved in 2-ethylhexanoic acid and hexamethyldisiloxane as precursors (11,14,15) resulted in nanoparticles of 20 to 75 nm size (Figure 1). Prior to exposure, all materials were thoroughly characterized for composition, shape and size distribution. As-prepared nanoparticles were dispersed in ultra-pure water (Millipore, resistivity > 18.2 MΩ cm<sup>-1</sup>) to prepare stock dispersions of 3000 parts per million (corresponds to µg particles per ml cell culture medium; further referred to as ppm). Prior to use, dispersions were sonicated for 10 min in an ultrasonic bath (600 Watt, Sonorex RK 156 BH, Bandelin). No artificial or additional detergents were used as to provide conditions as close as possible to an accidental pulmonary dust uptake of engineered nanoparticles.

*Physical properties of nanoparticles.* The specific surface area (SSA) and mean primary particle diameter of the as-synthesized nanopowders were measured on a Tristar (Micromeritics Instruments) by nitrogen adsorption at 77 K using the Brunauer-Emmett-Teller (BET) method. Samples were out-gassed at 150 °C for 1 hour prior to analysis. The average BET-equivalent particle diameter  $d_{\text{BET}}$  was calculated according to  $d_{\text{BET}} = 6 / (\text{SSA} \cdot \rho)$ , where  $\rho$  denotes the material density (kg m<sup>-3</sup>) and assuming monodisperse particles. Particle size distributions were measured using an X-ray disc centrifuge (XDC, Brookhaven Instruments) applying 1 wt% particle suspensions in water following a procedure outlined earlier (16). X-ray powder diffraction (XRD) patterns were collected on a Bruker D 8 Advance diffractometer from 15 ° to 50 ° at a step size of 0.12 ° and a scan speed of 2.4 ° min<sup>-1</sup> at ambient condition to confirm identity and crystallinity of all investigated materials (see Supplementary Figure S3 for all XRD pattern).

*Surface Charge Measurements.* To analyze the stability of nanoparticle suspensions in the present in vitro investigation, zeta-potential measurements were preformed by the colloidal vibration current method (Dispersion Technologie DT 1200). The zeta-potential was measured from 20 ml 4wt% metal oxide suspensions in water mixed with 20 ml HBSS, which was incubated prior to the measurements for four hours to a proportional amount of A 549 cells as in the *in vitro* experiments.

*Particle morphology and homogeneity.* Particle shape and morphology were investigated by transmission electron microscopy (TEM) recorded on a CM30 ST (Philips, LaB6 cathode, operated at 300 kV, point resolution 2 Å). Uniformity of the materials was investigated by scanning transmission electron microscopy (STEM) and by laser ablation inductively coupled plasma mass spectroscopy (LA ICP-MS). Scanning transmission electron microscopy (STEM) investigations were performed on a Tecnai F30 microscope (FEI (Eindhoven); field emission cathode, operated at 300 kV). Scanning transmission electron microscopy (STEM) images, obtained with a high-angle annular dark field (HAADF) detector, reveal the heavy particle constituents (e.g. iron oxide domains) with bright contrast (Z contrast). For qualitative analysis by energy dispersive

X-ray spectroscopy (EDXS) an additional detector (EDAX) was attached to the Tecnai F30 microscope and the focussed electron beam was then set on selected areas.

*Chemical composition* The chemical composition analysis of pressed pills was carried out using an 193 nm ArF excimer laser ablation system (Lambda Physik, Göttingen Germany) coupled to an ICP-MS (DRC II +, Perkin Elmer, Norwalk, USA) following a procedure described earlier (17). The samples were ablated for 60 s (10 Hz, 60 and 80  $\mu\text{m}$  crater diameter). The reference material NIST 610 was used as external calibration standard. Data reduction and concentration calculations were carried out using a protocol as described by Longerich et al. (18).

*Cell culture and exposure to nanoparticles.* Epithelial cells A549 (ATCC, CCL-185) further referred to as A549, were cultivated in T25 flasks (TTP, Trasadingen, Switzerland) with RPMI-1640 medium (Sigma-Aldrich, Buchs, Switzerland) containing 10 % fetal calf serum (Invitrogen AG, Basel, Switzerland) and 1 % penicillin-streptomycin-neomycin antibiotic mixture (PSN, 5 mg  $\text{mL}^{-1}$  penicillin, 5 mg  $\text{mL}^{-1}$  streptomycin, and 10 mg  $\text{mL}^{-1}$  neomycin, Invitrogen AG, Basel, Switzerland) at 37 °C in a humidified atmosphere of 5% CO<sub>2</sub> in air (19-21). Before exposure experiments, cells near confluence were trypsinized and transferred at a concentration of 20'000 cell per well into 96-well cultivation (TTP, Switzerland) plates.

After 1 day in culture, the medium was replaced by 100  $\mu\text{L}$  of HBSS buffer (Hanks' Balanced Salt Solution (22)) with 50  $\mu\text{M}$  HDCF-DA (D-399, Molecular Probes, Invitrogen) and kept in dark (23) for one hour. Cells were then washed three times with pure HBSS buffer and exposed to particle suspensions following a procedure most recently developed by Brunner et. al. (21). Immediately before cell exposure, aqueous nanoparticles suspensions (1000 ppm) were diluted in HBSS to the final concentration of 30 ppm (30  $\mu\text{g mL}^{-1}$ ) by adding 100  $\mu\text{L}$  of stock dispersion to the corresponding well. Cells containing only HBSS and no particles were used as negative control and as reference. SIN-1 (3-morpholino-syndnonimine hydrochloride, Sigma) was employed as a radical producing positive control (24-26). The amount of generated fluorescein DCF (supporting information, Figure S6) was measured after 4 hours by the fluorescence signal strength F at 528 nm using an excitation at 485 nm (FL800, BioTek). The relative amount of expressed ROS (%) compared to cultures without exposure to nanoparticles was calculated by  $(F \text{ test}) / (F \text{ reference}) \times 100$ . For ion control experiments, FeCl<sub>3</sub> (Fluka, purum), MnCl<sub>2</sub> (Merck, purum) and CoCl<sub>2</sub> (Chemie Brunschwig, purum) were used at metal concentrations corresponding to the nanoparticles suspensions (see Table ST 3 for detailed salt concentrations,). No salt controls were made for titania as latter can not be dissolved in neutral biological media due to the chemical behavior of titanium.

*ROS production by catalytically active nanoparticles.* In order to quantify the ROS generation in the absence of living cells, we exposed both HDCF and HDCF-DA to nanoparticles dispersions. Earlier occurred errors with the application of microbiological assays on nanomaterial containing cell cultures motivate for such careful control experiments (27-29). The free, reduced dye (active form; HDCF) was freshly produced from HDCF-DA according to Carthcart et al. (30,31). In 96-well plates, 100  $\mu\text{L}$  of a suspension containing 60 ppm particles in HBSS buffer were mixed with 100  $\mu\text{L}$  of a

solution containing 50 µM deesterified dye HDCF. After four hours, the amount of generated fluorescein (DCF, supporting information, Figure S6) was measured by fluorescence (FL800, BioTek). This procedure is further called oxygen control and provided the amount of ROS generated by nanoparticles in the absence of living cells. Use of the reactive form of the dye assured a fair control experiment. As chemically inert reference, pure silica or pure HBSS buffer were used. Cell free experiments preformed with nanoparticles and HDCF-DA showed no dye oxidation since the ester form was not susceptible to oxidation. It can therefore be safely assumed, that nanoparticles outside of the cell can not transform HDCF-DA to HDCF and further to DCF. Therefore, extra-cellular dye and nanoparticles can not contribute to the observed DCF formation.

*Catalytical activity for H<sub>2</sub>O<sub>2</sub> decomposition.* Since intracellular hydrogen peroxide (H<sub>2</sub>O<sub>2</sub>) may also account for ROS generation on living cells (3), the ROS level of nanoparticles suspensions were further measured using the same procedure as for the oxygen control but with additional hydrogen peroxide (Merck, p.a.) concentration of 0.15 wt%. Next to abundant technical literature on the catalytic activity of the investigated materials (32-37) the degradation rate was used as a measure for catalytic activity (38). First, dispersions of 40 mg of particles in 20 ml water were prepared by ultra-sonication (Sonorex RK 156 BH, Bandelin). Afterwards 0.1 ml H<sub>2</sub>O<sub>2</sub> (Merck, Germany) was diluted to 1.5 wt% H<sub>2</sub>O<sub>2</sub> in water for 1.6 wt% cobalt/silica or to 0.15 wt% H<sub>2</sub>O<sub>2</sub> in water for the other materials. After 3 hours stirring at room temperatures in the dark the suspensions were centrifuged for 15 minutes at 20'000 g to remove all particles. In a volumetric flask, two milliliters of the supernatant were added to 10 ml 5 wt% H<sub>2</sub>SO<sub>4</sub> (Fluka, Germany) and then diluted with water to 100 ml. The remaining H<sub>2</sub>O<sub>2</sub> was determined by titration with 0.02 M potassium permanganate (Tritisol, Merck) following a procedure outlined in (38).

*Statistics and data representation.* For all figures relative ROS generation data were represented as (mean values ± standard error of the mean values) over (mean experimental values) relative to untreated controls for cell cultures experiments and relative to silica for cell free experiments. Statistically significant data sets were indicated by a star \* for p < 0.05 using a student's t-test.

## Supplementary results

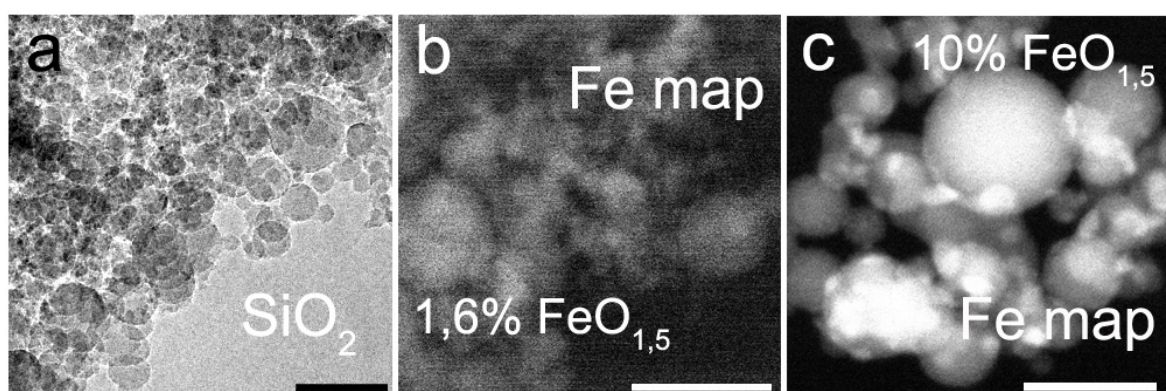
### Particle characterization

*Homogeneity and composition.* The particle homogeneity and composition was tested as described by Limbach et al. (16) and Stark et al. (33) and revealed a high purity and sample homogeneity (13). The comparison of selected samples for nominal versus measured composition by laser ablation ion coupled plasma mass spectroscopy corroborated an excellent agreement between precursors composition and product composition as typical for flame spray synthesis (13,39).

**Supplementary Table ST1. Measured metal content in flame made nanoparticles.**

Nominal composition in the liquid feed	Measured element composition in the product nanoparticles
1.6% FeO <sub>1,5</sub> / SiO <sub>2</sub>	1.57% +/- 0.08
1.6% MnO <sub>1,5</sub> / SiO <sub>2</sub>	1.58% +/- 0.02
1.6% CoO <sub>4/3</sub> / SiO <sub>2</sub>	1.52% +/- 0.09

*Particle Morphology.* Scanning transmission electron micrographs (STEM) were used to probe the element distribution of iron doped silica. In agreement with earlier investigations on the catalytic properties of iron/silica, Supplementary Figure S2 revealed a smooth iron oxide distribution (Fe map shows exclusively Fe atoms) at low Fe doping concentrations (1.6% iron on silica) whereas in the case of higher Fe loadings (10% iron on silica) iron-rich regions were discernible as bright spots in the Fe map. This phase segregation is in full agreement with earlier investigations on Fe solubility in silica.



*Supplementary Figure S2.* (a) Transmission electron micrograph of silica. (b) Scanning transmission electron micrograph of 1.6% FeO<sub>1,5</sub> on SiO<sub>2</sub> and (c) 10% FeO<sub>1,5</sub> on SiO<sub>2</sub>. Size bar = 50 nm.

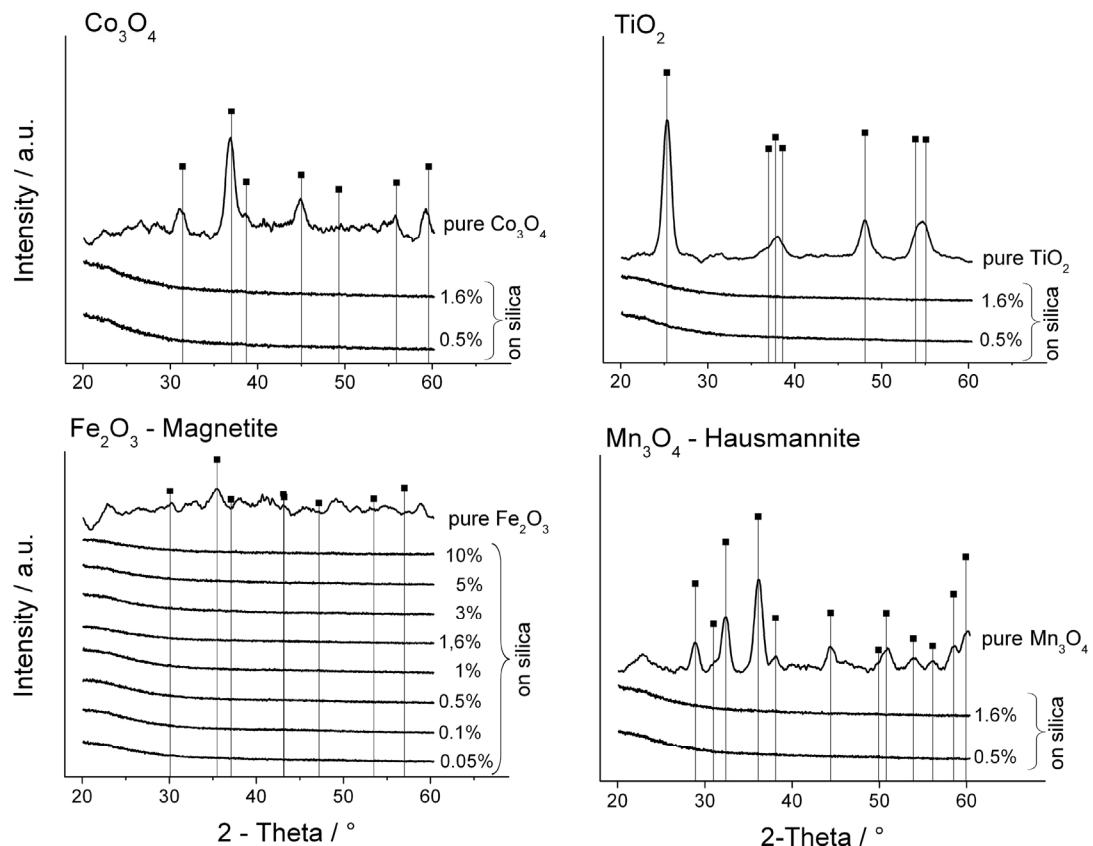
*Surface area.* The specific surface area of all investigated materials is showed in the supplementary table ST2. Assuming the specific density for compositions as a linear combination of their constituents and considering particles as spherical, the particle diameter  $d_{BET}$  can be calculated according to Brunner et al. (13).

**Supplementary Table ST2. Particle specific surface area, calculated diameter  $d_{BET}$  and particle surface/number dose during exposure.**

Materials	BET surface area / [m <sup>2</sup> /g]	Amount of surface of nanoparticles <sup>a</sup> / [10 <sup>-3</sup> m <sup>2</sup> /ml]	Primary particle diameter $d_{BET}$ / [10 <sup>-9</sup> m]	Primary particles per volume <sup>a</sup> / [10 <sup>12</sup> /ml]
SiO <sub>2</sub>	209	6.3	11.3	16
0.05% FeO <sub>1,5</sub> / SiO <sub>2</sub>	263	7.9	9.0	31
0.1% FeO <sub>1,5</sub> / SiO <sub>2</sub>	270	8.1	8.8	34
0.5% FeO <sub>1,5</sub> / SiO <sub>2</sub>	263	7.9	9.0	31
1% FeO <sub>1,5</sub> / SiO <sub>2</sub>	210	6.3	11.2	16
1.6% FeO <sub>1,5</sub> / SiO <sub>2</sub>	201	6.0	11.6	14
3% FeO <sub>1,5</sub> / SiO <sub>2</sub>	146	4.4	15.7	5.6
5% FeO <sub>1,5</sub> / SiO <sub>2</sub>	137	4.1	16.4	4.9
10% FeO <sub>1,5</sub> / SiO <sub>2</sub>	100	3.3	21.4	2.1
Fe <sub>2</sub> O <sub>3</sub>	93	2.8	12.3	5.9
0.5% MnO <sub>1,5</sub> / SiO <sub>2</sub>	227	6.8	10.3	20
1.6% MnO <sub>1,5</sub> / SiO <sub>2</sub>	170	5.1	13.7	8.6
Mn <sub>2</sub> O <sub>3</sub>	98	2.9	12.2	5.1
0.5% CoO <sub>4/3</sub> / SiO <sub>2</sub>	243	7.3	9.6	25
1.6% CoO <sub>4/3</sub> / SiO <sub>2</sub>	184	5.5	12.6	11
Co <sub>3</sub> O <sub>4</sub>	86	2.6	11.4	7.7
0.5% TiO <sub>2</sub> / SiO <sub>2</sub>	250	7.5	9.4	27
1.6% TiO <sub>2</sub> / SiO <sub>2</sub>	234	7.0	10.0	22
TiO <sub>2</sub>	118	3.5	12.0	7.8

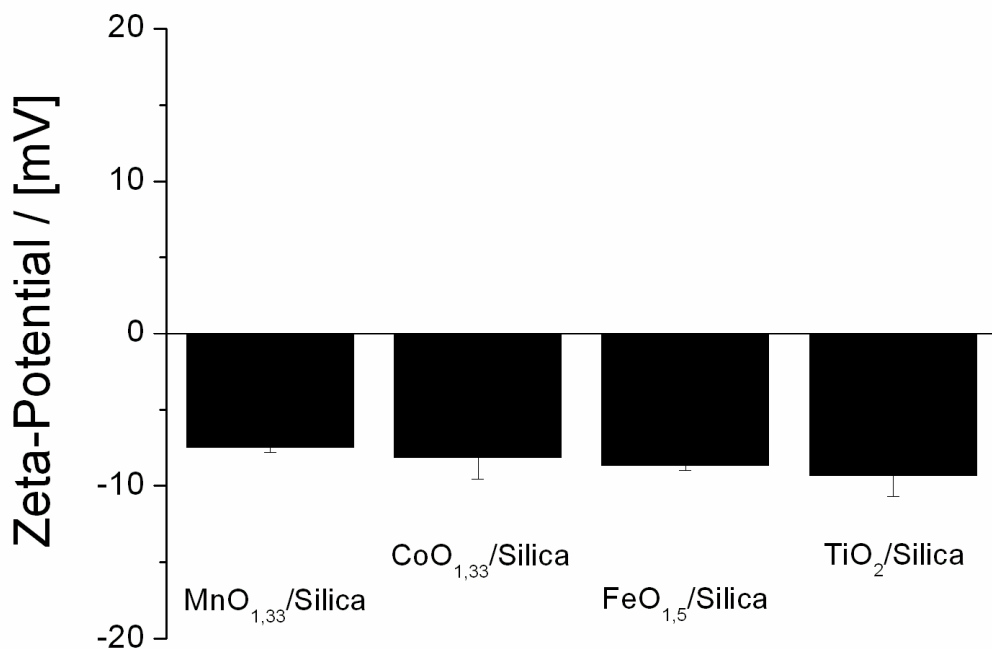
<sup>a</sup> Calculated specific surface area of nanoparticles present during exposure and number concentration expressed as primary particles per volume.

*Crystallinity and phase composition.* The phase composition of all samples was measured by X-ray diffraction (XRD). All silica based nanoparticles were fully amorphous independent of the dopant metal. Pure oxide showed partial crystallinity. Cobalt oxide ( $\text{Co}_3\text{O}_4$ ), titania ( $\text{TiO}_2$ , anatase) and manganese oxide ( $\text{Mn}_3\text{O}_4$ , Hausmannite) showed high crystallinity while iron oxide nanoparticles showed only small reflections that could be assigned to the magnetite phase.



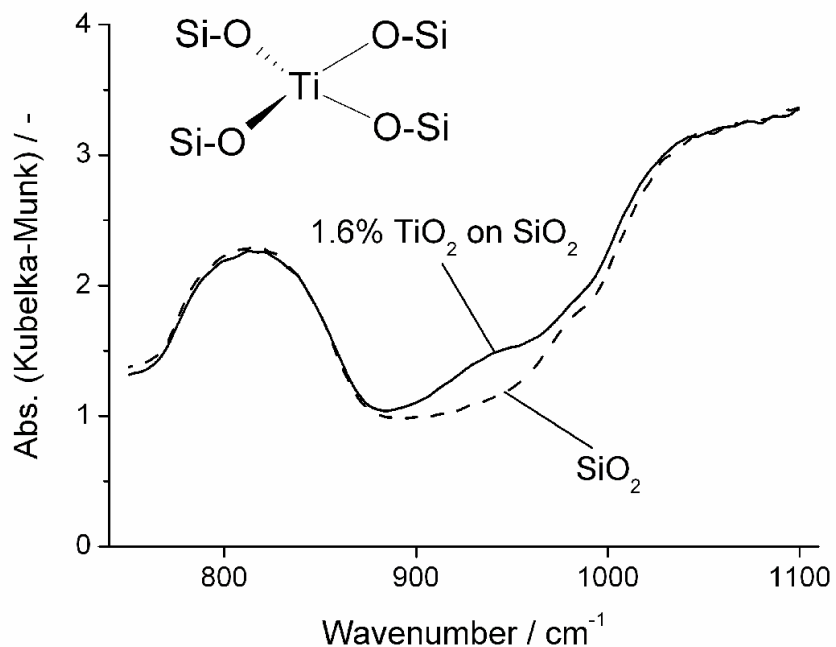
*Supplementary Figure S3. Phase composition as measured by X-ray diffraction patterns of as-prepared nanoparticles.*

*Zeta potential of different doped silica nanoparticles.* In order to back up the assumption of similar uptake rate according to (16), the zeta potentials of doped silica nanoparticles were measured in a exactly the same medium as the exposure to the living cells was carried out. The medium was taken from cell culture supernatants treated with saline controls instead of particle suspensions. The zeta potential was recorded within minutes after the addition of the particles and remained unchanged afterwards.



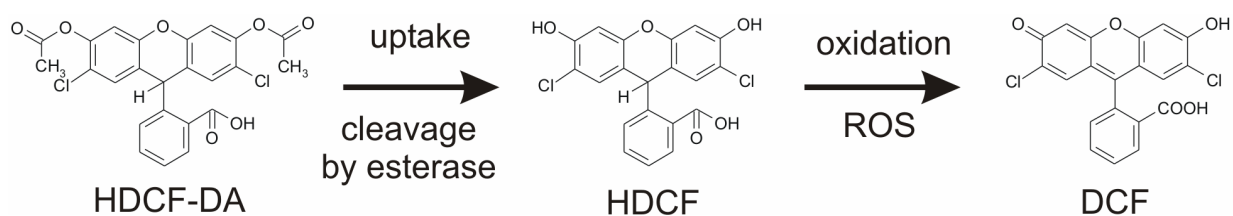
*Supplementary Figure S4. Zeta potentials of different transition metal doped silica nanoparticles samples (all dopant concentrations were 1.6 wt% transition metal oxide). This high degree of similarity justifies the assumption of similar rates of uptake into the in vitro cell cultures as shown previously by Limbach et al. (16).*

*Structure of the transition metal ions in silica.* Diffuse reflectance Fourier transform Infrared spectroscopy (DRIFTS) recorded on a Bruker Sensor 27 with heat control and gas flow (Pike Technology, Auto Pro) was used to probe the geometry of the transition metal ions in the silica matrix. Samples were diluted in KBr (Fluka) and measured against a KBr background from 4000 to 400  $\text{cm}^{-1}$  at 300 °C with flowing nitrogen.



*Supplementary Figure S5. In-situ diffuse reflectance Fourier transform Infrared spectra of silica and 1.6%  $\text{TiO}_2$  on silica. Ti-O-Si bonds corroborated the presence of tetrahedral sites as typically found in heterogeneous catalysts of such composition and resulted in a shoulder at 960  $\text{cm}^{-1}$ .*

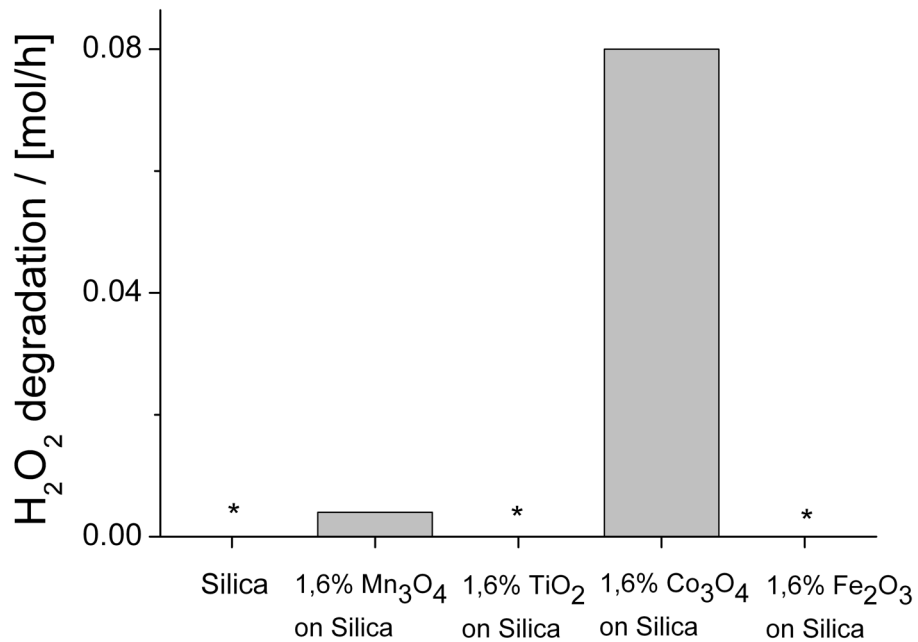
## Mechanism of the ROS assay



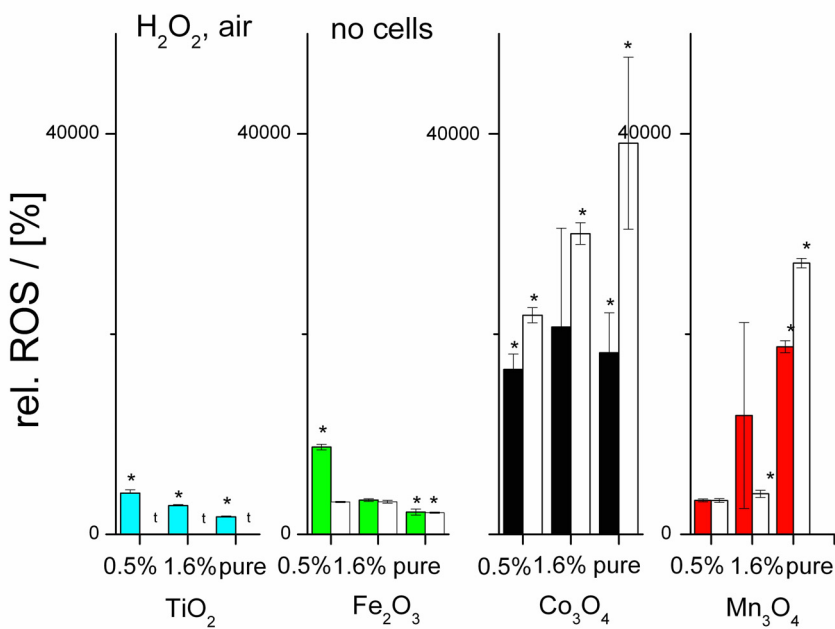
*Supplementary Figure S6. The use of di-chloro-fluorescein provides a sensitive probe for ROS inside a cell. The esterified form of the reduced dye (HDCF-DA) is readily taken up by living cells where the acetate is cleaved off in the cytosol and results in the release of the active probe (non-fluorescent HDCF). Selective oxidation by ROS yields strongly fluorescent DCF. This reaction sequence allows a distinction between reaction out or inside of a cell since HDCF-DA does not react with ROS.*

## Oxygen or hydrogen peroxide as a source for ROS formation

The formation of ROS in a direct, chemical pathway needs a source of oxidation precursors. Both molecular oxygen and hydrogen peroxide (naturally occurring; intracellularly formed from the action of superoxide dismutase on the superoxide radical) could serve as precursors. Using only air (1<sup>st</sup> series of control experiments, Figure 4) or additional H<sub>2</sub>O<sub>2</sub> (2<sup>nd</sup> series of control experiments, supporting information, Figure S8) displayed strongly contrasting activity. While the relative ROS levels in air control experiments (Figure 4) clearly followed the ROS levels found within cultures (Figure 2), the activity pattern in control experiments with additional H<sub>2</sub>O<sub>2</sub> showed a very different reactivity. Cobalt containing silica nanoparticles were extremely active for ROS formation and the about 100 times higher levels confirm that H<sub>2</sub>O<sub>2</sub> can not be regarded as a significant precursor for intracellular ROS from a direct pathway (supporting information, Figure S1). If hydrogen peroxide was important for ROS generation, the relative ROS levels in exposed cell cultures (Figure 2) would have to reflect at least in parts the reactivity pattern in the cell free, H<sub>2</sub>O<sub>2</sub> environment (supporting information, Figure S8). The pronounced activity of cobalt is in line with studies on Co(II) complexes that generated oxygen-based radicals from a reaction with hydrogen peroxides under physiological conditions (40).



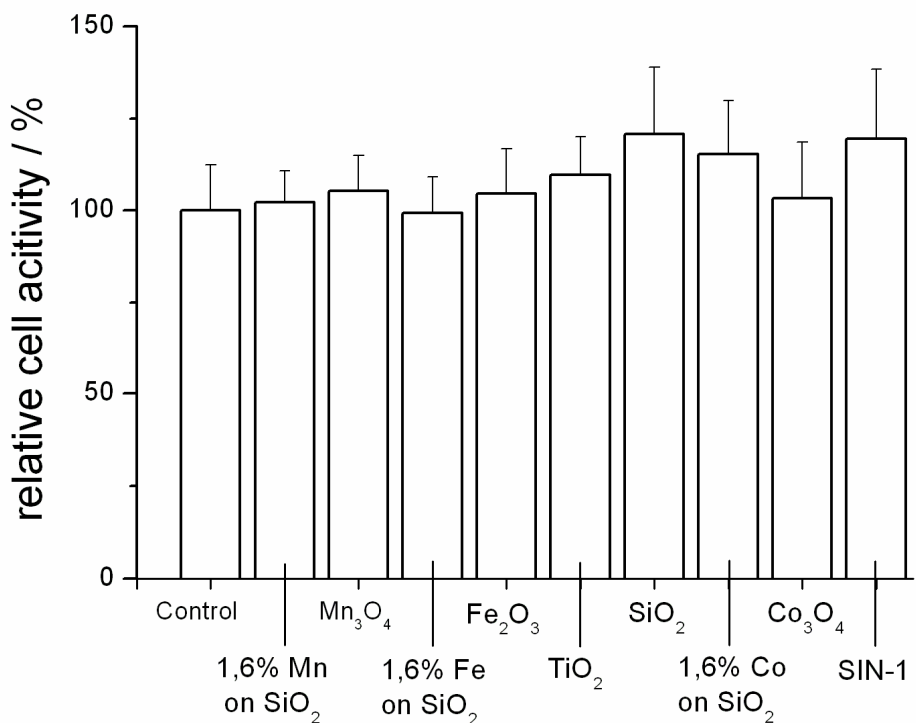
*Supplementary Figure S7. Hydrogen peroxide degradation of selected materials revealed a pronounced activity in the case of cobalt. (\* values for silica, Ti-silica and Fe-silica were below detection limit using titration.)*



*Supplementary Figure S8. Control experiment on the ROS formation without cells testing the role of hydrogen peroxide as a source for ROS. The relative activity of all investigated materials and the reference salts show a distinctly different pattern than the in vitro investigations (Figures 2 and 3). This clearly shows that the ROS were generated using oxygen as a major source while intracellular  $\text{H}_2\text{O}_2$  is of negligible importance.*

## Control of cellular viability during experiments

In order to distinguish between acute toxic effects involving loss of cell viability and the ROS generation in well proliferating cells, the cellular metabolism was measured quantitatively using a MTT-assay following a procedure by Brunner et al. (21). Within four hours of exposure (duration of the experiments) no statistically significant decrease in cell activity was found.



*Supplementary Figure S9. Cell activity measurements (MTT-assay) after 4h exposure to nanoparticles showed no significant loss in cell activity if compared to untreated controls.*

## **Composition of HBSS buffer**

Hanks' Balanced Salt Solution contained on a liter basis:

1 g D-Glucose	(Sigma G7528, sigma ultra 99.5%)
0.185g CaCl <sub>2</sub> * 2H <sub>2</sub> O	(Merck 1.02382.0500 pro analysis)
0.4g KCl	(Fluka 60130 p.a.)
0.06g KH <sub>2</sub> PO <sub>4</sub>	(Fluka 60220 p.a.)
0.1g MgCl <sub>2</sub> * 6H <sub>2</sub> O	(Fluka 63068 ultra mol biology)
0.1g MgSO <sub>4</sub> * 7H <sub>2</sub> O	(Fluka 63138 micro select)
8.0g NaCl	(Fluka 71380 p.a.)
0.35 g NaHCO <sub>3</sub>	(Fluka 71628 p.a.)
0.06 g Na <sub>2</sub> HPO <sub>4</sub> * 2H <sub>2</sub> O	(Fluka 71644 ultra)

The acidity was adjusted to a pH of 7.4.

## **Reference exposure concentrations for metal salts**

**Supplementary Table ST3. Reference exposure concentrations for metal salts.**

salt reference <sup>a</sup>	concentration	corresponding to
FeCl <sub>3</sub>	0.371 mM	30 ppm Fe <sub>2</sub> O <sub>3</sub>
MnCl <sub>2</sub>	0.393 mM	30 ppm Mn <sub>3</sub> O <sub>4</sub>
CoCl <sub>2</sub>	0.374 mM	30 ppm Co <sub>3</sub> O <sub>4</sub>

<sup>a</sup> No soluble titania salts are known for neutral, aqueous systems.

Note: Total metal content of oxide nanoparticles or salts is constant.

## Supplementary Literature

- (1) Halliwell, B.; Whiteman, M. Measuring reactive species and oxidative damage in vivo and in cell culture: how should you do it and what do the results mean? *Br. J. Pharmacol.* **2004**, *142*, 231-255.
- (2) Chance, B.; Sies, H.; Boveris, A. Hydroperoxide metabolism in mammalian organs. *Physiol. Rev.* **1979**, *59*, 527-605.
- (3) Halliwell, B.; Gutteridge, J. M. C. Role of free-radicals and catalytic metal-ions in human-disease - an overview. *Method Enzymol.* **1990**, *186*, 1-85.
- (4) Sohal, R. S. Oxidative stress hypothesis of aging. *Free Radic. Biol. Med.* **2002**, *33*, 573-574.
- (5) Butterfield, D. A. Proteomics: a new approach to investigate oxidative stress in Alzheimer's disease brain. *Brain Res.* **2004**, *1000*, 1-7.
- (6) Markesberry, W. R. Oxidative stress hypothesis in Alzheimer's disease. *Free Radic. Biol. Med.* **1997**, *23*, 134-147.
- (7) Brownlee, M. Biochemistry and molecular cell biology of diabetic complications. *Nature* **2001**, *414*, 813-820.
- (8) Yu, T. Z.; Robotham, J. L.; Yoon, Y. Increased production of reactive oxygen species in hyperglycemic conditions requires dynamic change of mitochondrial morphology. *Proc. Natl. Acad. Sci. U. S. A.* **2006**, *103*, 2653-2658.
- (9) Jacobson, M. D. Reactive oxygen species and programmed cell death. *Trends Biochem. Sci.* **1996**, *21*, 83-86.
- (10) Loft, S.; Poulsen, H. E. Cancer risk and oxidative DNA damage in man. *J. Mol. Med.* **1996**, *74*, 297-312.
- (11) Loher, S.; Stark, W. J.; Maciejewski, M.; Baiker, A.; Pratsinis, S. E.; Reichardt, D.; Maspero, F.; Krumeich, F.; Gunther, D. Fluoro-apatite and calcium phosphate nanoparticles by flame synthesis. *Chem. Mat.* **2005**, *17*, 36-42.
- (12) Grass, R. N.; Stark, W. J. Flame synthesis of calcium-, strontium-, barium fluoride nanoparticles and sodium chloride. *Chem. Commun.* **2005**, 1767-1769.
- (13) Brunner, T. J.; Grass, R. N.; Stark, W. J. Glass and bioglass nanopowders by flame synthesis. *Chem. Commun.* **2006**, 1384-1386.
- (14) Stark, W. J.; Kammler, H. K.; Strobel, R.; Gunther, D.; Baiker, A.; Pratsinis, S. E. Flame-made titania/silica epoxidation catalysts: Toward large-scale production. *Ind. Eng. Chem. Res.* **2002**, *41*, 4921-4927.
- (15) Madler, L.; Kammler, H. K.; Mueller, R.; Pratsinis, S. E. Controlled synthesis of nanostructured particles by flame spray pyrolysis. *J. Aerosol. Sci.* **2002**, *33*, 369-389.
- (16) Limbach, L. K.; Li, Y. C.; Grass, R. N.; Brunner, T. J.; Hintermann, M. A.; Muller, M.; Gunther, D.; Stark, W. J. Oxide nanoparticle uptake in human lung fibroblasts: Effects of particle size, agglomeration, and diffusion at low concentrations. *Environ. Sci. Technol.* **2005**, *39*, 9370-9376.
- (17) Ottinger, F.; Kroslakova, I.; Hametner, K.; Reusser, E.; Nesper, R.; Gunther, D. Analytical evidence of amorphous microdomains within nitridosilicate and nitridoaluminosilicate single crystals. *Anal. Bioanal. Chem.* **2005**, *383*, 489-499.

- (18) Longerich, H. P.; Jackson, S. E.; Gunther, D. Laser ablation inductively coupled plasma mass spectrometric transient signal data acquisition and analyte concentration calculation. *J. Anal. At. Spectrom.* **1996**, *11*, 899-904.
- (19) Wotrich, R.; Diabate, S.; Krug, H. F. Biological effects of ultrafine model particles in human macrophages and epithelial cells in mono- and co-culture. *Int. J. Hyg. Environ. Health.* **2004**, *207*, 353-361.
- (20) Rothen-Rutishauser, B. M.; Kiama, S. G.; Gehr, P. A three-dimensional cellular model of the human respiratory tract to study the interaction with particles. *Am. J. Respir. Cell Mol. Biol.* **2005**, *32*, 281-289.
- (21) Brunner, T. J.; Wick, P.; Manser, P.; Spohn, P.; Grass, R. N.; Limbach, L. K.; Bruinink, A.; Stark, W. J. In vitro cytotoxicity of oxide nanoparticles: Comparison to asbestos, silica, and the effect of particle solubility. *Environ. Sci. Technol.* **2006**, *40*, 4374-4381.
- (22) Eagle, H. Amino Acid Metabolism in Mammalian Cell Cultures. *Science* **1959**, *130*, 432-437.
- (23) Grzelak, A.; Rychlik, B.; Baptosz, G. Light-dependent generation of reactive oxygen species in cell culture media. *Free Radic. Biol. Med.* **2001**, *30*, 1418-1425.
- (24) Keston, A. S.; Brandt, R. Fluorometric analysis of ultramicro quantities of hydrogen peroxide. *Anal. Biochem.* **1965**, *11*, 1-5.
- (25) Lipton, S. A.; Choi, Y. B.; Pan, Z. H.; Lei, S. Z. Z.; Chen, H. S. V.; Sucher, N. J.; Loscalzo, J.; Singel, D. J.; Stamler, J. S. A redox-based mechanism for the neuroprotective and neurodestructive effects of nitric-oxide and related nitroso-compounds. *Nature* **1993**, *364*, 626-632.
- (26) Wang, H.; Joseph, J. A. Quantifying cellular oxidative stress by dichlorofluorescein assay using microplate reader. *Free Radic. Biol. Med.* **1999**, *27*, 612-616.
- (27) O'Malley, Y. Q.; Reszka, K. J.; Britigan, B. E. Direct oxidation of 2',7'-dichlorodihydrofluorescein by pyocyanin and other redox-active compounds independent of reactive oxygen species production. *Free Radic. Biol. Med.* **2004**, *36*, 90-100.
- (28) Worle-Knirsch, J. M.; Pulskamp, K.; Krug, H. F. Oops they did it again! Carbon nanotubes hoax scientists in viability assays. *Nano Lett.* **2006**, *6*, 1261-1268.
- (29) Wrona, M.; Wardman, P. Properties of the radical intermediate obtained on oxidation of 2',7'-dichlorodihydrofluorescein, a probe for oxidative stress. *Free Radic. Biol. Med.* **2006**, *41*, 657-667.
- (30) Cathcart, R.; Schwiers, E.; Ames, B. N. Detection of picomole levels of hydroperoxides using a fluorescent dichlorofluorescein assay. *Anal. Biochem.* **1983**, *134*, 111-116.
- (31) LeBel, C. P.; Ischiropoulos, H.; C., B. S. Evaluation of the probe 2',7'-dichlorofluorescin as an indicator of reactive oxygen species formation and oxidative stress. *Chem. Res. Toxicol.* **1992**, *5*, 227-231.
- (32) Sheldon, R. A. Homogeneous and heterogeneous catalytic oxidations with peroxide reagents. *Top. Curr. Chem.* **1993**, *164*, 21-43.
- (33) Stark, W. J.; Strobel, R.; Gunther, D.; Pratsinis, S. E.; Baiker, A. Titania-silica doped with transition metals via flame synthesis: structural properties and catalytic behavior in epoxidation. *J. Mater. Chem.* **2002**, *12*, 3620-3625.

- (34) Hutter, R.; Mallat, T.; Baiker, A. Titania-silica mixed oxides. 2. Catalytic behavior in olefin epoxidation. *J. Catal.* **1995**, *153*, 177-189.
- (35) Dutoit, D. C. M.; Schneider, M.; Baiker, A. Titania-silica mixed oxides. 1. Influence of sol-gel and drying conditions on structural-properties. *J. Catal.* **1995**, *153*, 165-176.
- (36) Fabrizioli, P.; Burgi, T.; Baiker, A. Environmental catalysis on iron oxide-silica aerogels: Selective oxidation of NH<sub>3</sub> and reduction of NO by NH<sub>3</sub>. *J. Catal.* **2002**, *206*, 143-154.
- (37) Fabrizioli, P.; Burgi, T.; Burgener, M.; van Doorslaer, S.; Baiker, A. Synthesis, structural and chemical properties of iron oxide-silica aerogels. *J. Mater. Chem.* **2002**, *12*, 619-630.
- (38) Zhou, H.; Shen, Y. F.; Wang, J. Y.; Chen, X.; O'Young, C. L.; Suib, S. L. Studies of decomposition of H<sub>2</sub>O<sub>2</sub> over manganese oxide octahedral molecular sieve materials. *J. Catal.* **1998**, *176*, 321-328.
- (39) Stark, W. J.; Madler, L.; Maciejewski, M.; Pratsinis, S. E.; Baiker, A. Flame synthesis of nanocrystalline ceria-zirconia: effect of carrier liquid. *Chem. Commun.* **2003**, 588-589.
- (40) Valko, M.; Rhodes, C. J.; Moncol, J.; Izakovic, M.; Mazur, M. Free radicals, metals and antioxidants in oxidative stress-induced cancer. *Chem.-Biol. Interact.* **2006**, *160*, 1-40.